the plant journal

SEB SOCIETY FOR EXPERIMENTAL BIOLOGY

The Plant Journal (2024) doi: 10.1111/tpj.16688

The TRAPPIII subunit, Trs85, has a dual role in the trafficking of cellulose synthase complexes in *Arabidopsis*

Holly Allen, Xiaoyu Zhu, Shundai Li* and Ying Gu*

Department of Biochemistry and Molecular Biology, Pennsylvania State University, University Park, Pennsylvania 16802, USA

Received 18 October 2023; revised 24 January 2024; accepted 29 January 2024.
*For correspondence (e-mail sul38@psu.edu; yug13@psu.edu).

SUMMARY

Plant cell walls are essential for defining plant growth and development, providing structural support to the main body and responding to abiotic and biotic cues. Cellulose, the main structural polymer of plant cell walls, is synthesized at the plasma membrane by cellulose synthase complexes (CSCs). The construction and transport of CSCs to and from the plasma membrane is poorly understood but is known to rely on the coordinated activity of cellulose synthase-interactive protein 1 (CSI1), a key regulator of CSC trafficking. In this study, we found that Trs85, a TRAPPIII complex subunit, interacted with CSI1 *in vitro*. Using functional genetics and live-cell imaging, we have shown that *trs85-1* mutants have reduced cellulose content, stimulated CSC delivery, an increased population of static CSCs and deficient clathrin-mediated endocytosis in the primary cell wall. Overall, our findings suggest that Trs85 has a dual role in the trafficking of CSCs, by negatively regulating the exocytosis and clathrin-mediated endocytosis of CSCs.

Keywords: cellulose synthase complex trafficking, TRAPPIII complex, Trs85, live-cell imaging, exocytosis, endocytosis.

INTRODUCTION

All plant cells are encased by a polysaccharide-rich primary cell wall that consists of cellulose, hemicellulose and pectin contained in an interlinking matrix. In contrast to hemicellulose and pectin, which are synthesized in the Golgi, cellulose is synthesized *in situ* at the plasma membrane by hexameric cellulose synthase complexes (CSCs). CSCs consist of 18–24 cellulose synthase proteins (CESAs) (Nixon et al., 2016; Thomas et al., 2012; Vandavasi et al., 2016) that are hypothesized to each synthesize a single glucan chain that coalesce to form cellulose microfibrils (Morgan et al., 2013; Purushotham et al., 2020). As CSCs move through the plasma membrane, they extrude cellulose microfibrils directly into the cell wall. As a result, the regulation of cellulose synthesis is largely determined by the dynamics and trafficking of CSCs to the plasma membrane.

The assembly of CESA proteins into CSCs occurs in the endoplasmic reticulum (ER), or the Golgi, with the aid of STELLO proteins, before they are delivered to the plasma membrane (Zhang et al., 2016). CSCs are transported to sites on the plasma membrane that are marked by CSI1 proteins attached to microtubules, where they become inserted through coordinated interactions with PATROL1 and the exocyst complex (Zhu et al., 2018). Once successfully inserted, CSCs synthesize cellulose microfibrils as they migrate along the plasma membrane in parallel with underlying cortical microtubules (Li et al., 2016; Paredez et al., 2006). CSCs undergo endocytosis into the cytosol, where they are either transported for degradation, or they are recycled back to the plasma membrane. CSCs are largely internalized by clathrin-mediated endocytosis (CME); however, CSCs are still internalized in CME mutants, indicative of alternative endocytotic pathways (Li et al., 2016).

Many of these proteins linked with CSC trafficking were initially identified from gene co-expression analyses, mutant screens, co-immunoprecipitation analyses and yeast-2-hybrid assays (Gu et al., 2010; Polko et al., 2018; Vellosillo et al., 2021; Zhang et al., 2016; Zhu et al., 2018). Some of these proteins are homologous to trafficking proteins, originally described in yeast and mammals, suggesting that these pathways may be somewhat conserved in CSC trafficking. For instance, components of CME, a dominant form of endocytosis in mammals, are involved in CSC endocytosis (Bashline et al., 2013, 2015) and the exocyst complex, first described in budding yeast (Novick et al., 1980) is important in delivering CSCs to 'the lasma membrane' (Zhu et al., 2018).

Another important protein complex essential for trafficking in yeast and mammals is the TRAnsport Protein Particle (TRAPP) complex. TRAPP complexes are guanine exchange factors that switch on Rab GTPases by converting their bound GDP to GTP (Kim et al., 2016). Activated Rab GTPases recruit tethers that attract vesicles in the vicinity of their target membrane and subsequently promote fusion. TRAPP complexes were first identified in yeast as a mediator of ER to Golgi trafficking (Sacher et al., 1998). Since then, TRAPP complexes have been identified in many trafficking pathways in yeast, *Drosophilia*, mammals and more recently, *Arabidopsis*.

The general consensus is that two types of TRAPP complexes exist and function *in vivo*. TRAPPII complexes typically bind to Rab11 and mediate trafficking between the Golgi, trans-Golgi network (TGN) and plasma membrane (Thomas et al., 2019) and TRAPPIII complexes activate Rab1 GTPases during autophagy and TGN trafficking (Lynch-Day et al., 2010). Both types of TRAPP complexes are comprised of the same core subunits: Trs20, Trs23, Trs31, Trs33, Bet3 and Bet5, which can activate Rab GTPases *in vitro* (Galindo et al., 2021). However, TRAPPII and TRAPPIII complexes require additional subunits *in vivo* for correct functioning (Galindo et al., 2021; Riedel et al., 2018). In multicellular organisms, TRAPPII complexes typically associate with two larger subunits, Trs120 and Trs130, and TRAPPIII complexes associate with four subunits, Trs65, Trs85, TRAPPC11 and TRAPPC12.

Plant TRAPP complexes are hypothesized to resemble mammalian TRAPP complexes more closely than yeast since they are both multicellular, and the *Arabidopsis* genome contains homologs to the metazoan TRAPPIII subunits, TRAPPC11 and TRAPPC12, not found in yeast (Thellmann et al., 2010). The TRAPPII complex in *Arabidopsis* plays an important role in TGN/early endosome (EE) trafficking, endocytosis, exocytosis and protein sorting during cell plate formation in cytokinesis (Kalde et al., 2019; Ravikumar et al., 2018; Rybak et al., 2014). Bet5, a core TRAPP subunit, is required for meristem formation and pollen development (Zhang et al., 2018). The functional characterization of TRAPPIII subunits has also emerged in recent years. Another TRAPPIII-specific subunit, TRAPPC11, has been shown to have a role in TGN/EE integrity and the localization of TGN/EE markers, such as SYP61 (Rosquete et al., 2019). A TRAPPIII-specific subunit, Trs85, has been shown to modulate autophagy and virulence in *Magnaporthe oryzae* and regulate gravitropic response and PIN localization in *Arabidopsis* (Song et al., 2020; Wu et al., 2023). All TRAPPIII subunits have been identified in the Golgi and the TGN/EE (Drakakaki et al., 2012), a central hub for trafficking, including proteins involved with cellulose synthesis (Allen et al., 2021).

In this study, we investigated the role of Trs85, a TRAPPIII-specific subunit in CSC trafficking. Several subunits of the TRAPPIII complex were identified through a co-immunoprecipitation study of CSI1 that successfully revealed protein partners of CSC trafficking (Zhu et al., 2018). The direct interaction between CSI1 and Trs85 was revealed by an *in vitro* pull-down assay. In *trs85-1* mutants, YFP-CESA6 particles had reduced velocity, increased density and increased delivery at the plasma membrane, consistent with aberrant CSC trafficking. We also found that the delivery of YFP-CESA6 particles occurred more quickly after photobleaching and there was an increase in static particles in *trs85-1* mutants. CME dynamics were also perturbed in *trs85-1*. Our data suggest that Trs85 has a dual role in the trafficking of CSCs by influencing both the endocytosis and exocytosis of CSCs.

RESULTS

CSI1 interacts with Trs85 *in vitro*

Many novel CSC trafficking proteins have been identified through the co-immunoprecipitation of proteins that are integral components of CSCs (CESA6) or are associated with CSCs (CSI1). CSI1 is a central hub for CSC trafficking by bridging the interactions between multiple CSC trafficking proteins. A previous co-immunoprecipitation analysis of GFP-CSI1, focusing on *PATROL1* and the exocyst complex that co-purified with CSI1, proved very fruitful in identifying new regulating partners of CSC trafficking (Zhu et al., 2018). The TRAPP complex was also co-purified with GFP-CSI1, but not with the negative IgG controls in three biological replicates (Table S1). Specifically, three TRAPPIII-specific subunits (Trs85, TRAPPC11 and TRAPPC12), and all of the core TRAPP subunits except Bet5 were co-purified with GFP-CSI1 but not with the IgG controls (Table S1). The TRAPPII-specific subunits, Trs120 and Trs130, were not identified in the analysis.

We tested whether any of the TRAPP subunits specifically interacted with CSI1 using an *in vitro* pull-down assay. All TRAPP proteins that were identified in the co-immunoprecipitation experiments were tagged with GST, with the exception of Trs20 which could not be successfully cloned. GST-Trs85 successfully pulled down His-CSI1, and not empty His-purified proteins (Figure 1; Figure S1), further verifying the co-immunoprecipitation data and indicating a direct interaction between Trs85 and CSI1 (Table S1). No interactions between His-CSI1 and the GST-tagged proteins, Bet3, Trs23, Trs31, Trs33, Tca17, TRAPPC11 and TRAPPC12, were detected (Figure 1; Figure S1).

Cellulose content is reduced in the *trs85-1* primary cell wall

Since Trs85 could successfully pull-down CSI1 in our *in vitro* pull-downs, we decided to investigate whether Trs85 has a role in cellulose synthesis. A previous study reported

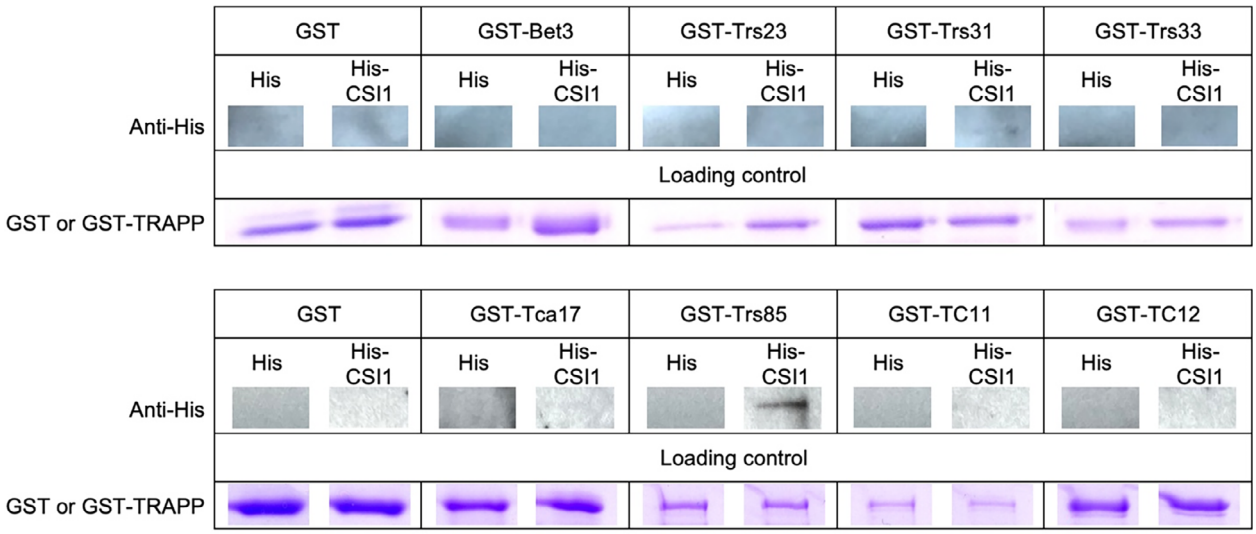

Figure 1. *In vitro* interactions between CSI1 and TRAPPIII complex proteins.
His-CSI1 was pulled down by GST-Trs85. No interactions were observed between His-CSI1 and GST-Bet3, GST-Trs23, GST-Trs31, GST-Trs33, GST-Tca17, GST-TRAPPC11 (GST-TC11) and GST-TRAPPC12 (GST-TC12). Interactions were performed between elution's of His-tagged proteins and GST-tagged proteins attached to beads. Loading controls show the quantity of His-elution and GST-beads added to each interaction. Empty GST- and His-vectors were used as negative controls. Results from one out of two reproducible independent experiments is shown. See also Figure S1.

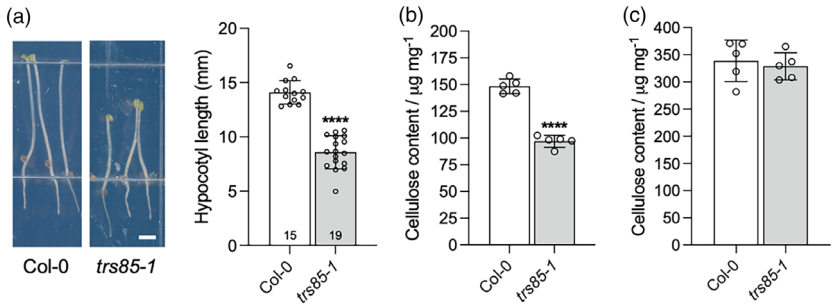

Figure 2. *trs85-1* knock-out mutants exhibit a cellulose deficient phenotype.
(a) Hypocotyl length of 4-day-old etiolated seedlings. The scale bar indicates 2 mm. Asterisks indicate significance (****$P \leq 0.0001$) based on a *t*-test. Numbers on bars indicate number of seedlings used. Bars show mean ± standard deviation.
(b, c) Cellulose content of (b) 4-day-old etiolated seedlings and (c) 6-week-old stems. Results from one out of three reproducible independent experiments is shown (a–c).

that four independent T-DNA insertions lines of Trs85 (referred to as DQC [defective quiescent centre]) had reduced gene expression of Trs85, and *dqc* seedlings exhibited shorter and wavy roots (Song et al., 2020). We found that *dqc-2* and *dqc-3* (referred to as *trs85-1* and *trs85-2* in this study) had identical phenotypes including shorter dark-grown hypocotyls, shorter roots in light-grown seedlings, reduced root hair, smaller rosette leaves and stunt adult plants (Figure S2). These mutant phenotypes were recapitulated in a *trs85-1 trs85-2* transheterozygote, demonstrating that *Trs85* is responsible for these defects (Figure S2). Both *trs85-1* and *trs85-2* were shown to have no expression of Trs85 (Song et al., 2020). We selected *trs85-1* for further analysis. To test whether the *trs85-1* mutation impacts cellulose synthesis, we measured the length and crystalline cellulose content of 4-day-old dark-grown hypocotyls. *trs85-1* mutants have significantly shorter hypocotyls and a lower crystalline cellulose content than the wild-type (Figure 2a,b). These are both phenotypes indicative of perturbations to cellulose synthesis in the primary cell wall. Since adult *trs85-1* plants have a smaller stature, we also quantified the cellulose content using 3″ of stem from the base of 6-week-old plant (material containing mainly secondary cell walls). *trs85-1* mutants exhibited no difference in cellulose content compared to the wild-type (Figure 2c). These results indicate that Trs85 may have a specific role in cellulose synthesis in the primary cell wall.

YFP-CESA6 dynamics are perturbed in *trs85-1*

To further investigate the role of Trs85 in cellulose synthesis in the primary cell wall, we crossed a line expressing a yellow fluorescent tagged CESA6 protein (YFP-CESA6) in the homozygous CESA6 null mutant background, *prc1-1*, with *trs85-1* (Figure S3). YFP-CESA6, which complements the *prc1-1* mutation, is a useful fluorescent marker that is frequently used to assess the dynamics, trafficking and regulation of CSCs at the plasma membrane (Allen et al., 2021; Paredez et al., 2006). We performed various live-cell imaging experiments with YFP-CESA6, *prc1-1* in the dark-grown hypocotyl to track the activity of CSCs. Firstly, we quantified the density of YFP-CESA6 particles at the plasma membrane to determine whether the delivery, or removal of CSCs, from the plasma membrane was perturbed in *prc1-1 trs85-1*. The density of YFP-CESA6 particles was significantly increased by 14% in *prc1-1 trs85-1* dark-grown hypocotyls, compared to *prc1-1* (Figure 3a,b). A higher density of YFP-CESA6 particles in *prc1-1 trs85-1* indicates a defect in CSC regulation that could either result from an increase in CSC secretion, a decrease in CSC internalization, or both.

Since cellulose content is reduced in *trs85-1*, we also quantified the velocity of YFP-CESA6 particles at the plasma membrane, a common proxy for the rate of cellulose synthesis (Diotallevi & Mulder, 2007; Paredez et al., 2006). The polymerization of cellulose is predicted to propel CSCs through the plasma membrane (Diotallevi & Mulder, 2007). The average velocity of YFP-CESA6 particles in *prc1-1 trs85-1* is 205.1 $\pm$ 73.68 nm min^{-1}, which is approximately 20% lower than in *prc1-1* where YFP-CESA6 particles had an average velocity of 252.2 $\pm$ 94.52 nm min^{-1} (Figure 3c,d; Movie S1). Slower CESA6 migration in *prc1-1 trs85-1* indicates that the reduced catalytic activity of CSCs may be responsible for the reduction in cellulose content (Figure 2b). Although a higher density of YFP-CESA6 at the plasma membrane may be expected to cause an increase in cellulose content, these CSCs may not be functional. Indeed, we observed a greater percentage of static YFP-CESA6 particles in *prc1-1 trs85-1* (16.12%) than in *prc1-1* (9.95%), which were excluded from the velocity analysis (Figure 3e; Movie S2). This population of immobile YFP-CESA6 particles may represent defective CSCs that have not successfully been inserted into the plasma membrane in *prc1-1 trs85-1* (Figure 3e).

Trs85 is required for the delivery of CSCs to the plasma membrane

TRAPPIII complexes have been shown to be involved in a variety of pathways including autophagy (Lynch-Day et al., 2010), Golgi and TGN/EE trafficking (Rosquete et al., 2018; Thomas et al., 2019) and endocytosis (Song et al., 2020). An altered density of YFP-CESA6 at the plasma membrane in *prc1-1 trs85-1* (Figure 3b), implicates a role for Trs85 in either, exocytosis, endocytosis, or both. CSI1 is an important protein for the docking of newly delivered CSCs to the plasma membrane during exocytosis (Zhu et al., 2018). Due to the interaction between Trs85 and CSI1 (Figure 1; Figure S1), we hypothesized that Trs85 may have a role in exocytosis and so we initially focused on this trafficking pathway. Additionally, *trs85-1* mutants have a root hair deficient phenotype (Figure S2) that is characteristic of other exocytotic mutants (Hála et al., 2008; Wen et al., 2005).

A common method for assessing the delivery of CSCs to the plasma membrane is Fluorescent Recovery After Photobleaching (FRAP). After photobleaching a specified region of the cell, the secretion of newly synthesized YFP-CESA6 particles to the plasma membrane can be easily observed and quantified over a time-lapse movie (Bashline et al., 2013; Zhu et al., 2018). We performed FRAP on YFP-CESA6, *prc1-1* and YFP-CESA6, *prc1-1 trs85-1* and determined the delivery rate of YFP-CESA6 to the plasma membrane over a period of 5 min. Unexpectedly, we noticed the appearance of many YFP-CESA6 particles in *prc1-1 trs85-1*, between 0 and 55 sec after photobleaching (Figure 4a,b; Movie S3), when they typically start to appear after 60 sec (Zhu et al., 2018). In *prc1-1 trs85-1*, approximately 33% of newly delivered YFP-CESA6 particles appeared within the first 55 sec after photobleaching, which is more than triple the percentage observed in control lines (10% in YFP-CESA6 *prc1-1*) (Figure 4b). On average, YFP-CESA6 particles appeared at the plasma membrane 43 sec earlier in *prc1-1 trs85-1* hypocotyls compared to *prc1-1* (Figure 4b).

Overall, the delivery rate of CSCs to the plasma membrane is five-fold higher in *prc1-1 trs85-1* compared to *prc1-1* (Figure 4c). Furthermore, a greater number of YFP-CESA6 particles can be observed at the plasma membrane in *prc1-1 trs85-1* after 5 min (Figure 4a; Movie S3), indicative of enhanced delivery. We defined a successful CSC delivery event as a YFP-CESA6 particle that paused for 80 $\pm$ 30 sec, before moving along a straight trajectory, as observed previously (Gutierrez et al., 2009; Zhu et al., 2018). We found that approximately 16% of YFP-CESA6 particles in *prc1-1 trs85-1*, remained static for over 110 sec, whereas only 9% of YFP-CESA6 particles in *prc1-1* exhibited an abnormally long pause phase (Figure 4d). A small fraction of YFP-CESA6 particles in *prc1-1 trs85-1*, remained static for almost the entire length of the movie (Figure 4d), suggesting more YFP-CESA6 particles exhibit abnormal dynamics in *prc1-1 trs85-1*. YFP-CESA6 particles with pause phases over 110 sec may reflect unsuccessful insertion events or insertions of dysfunctional CSCs into the plasma membrane.

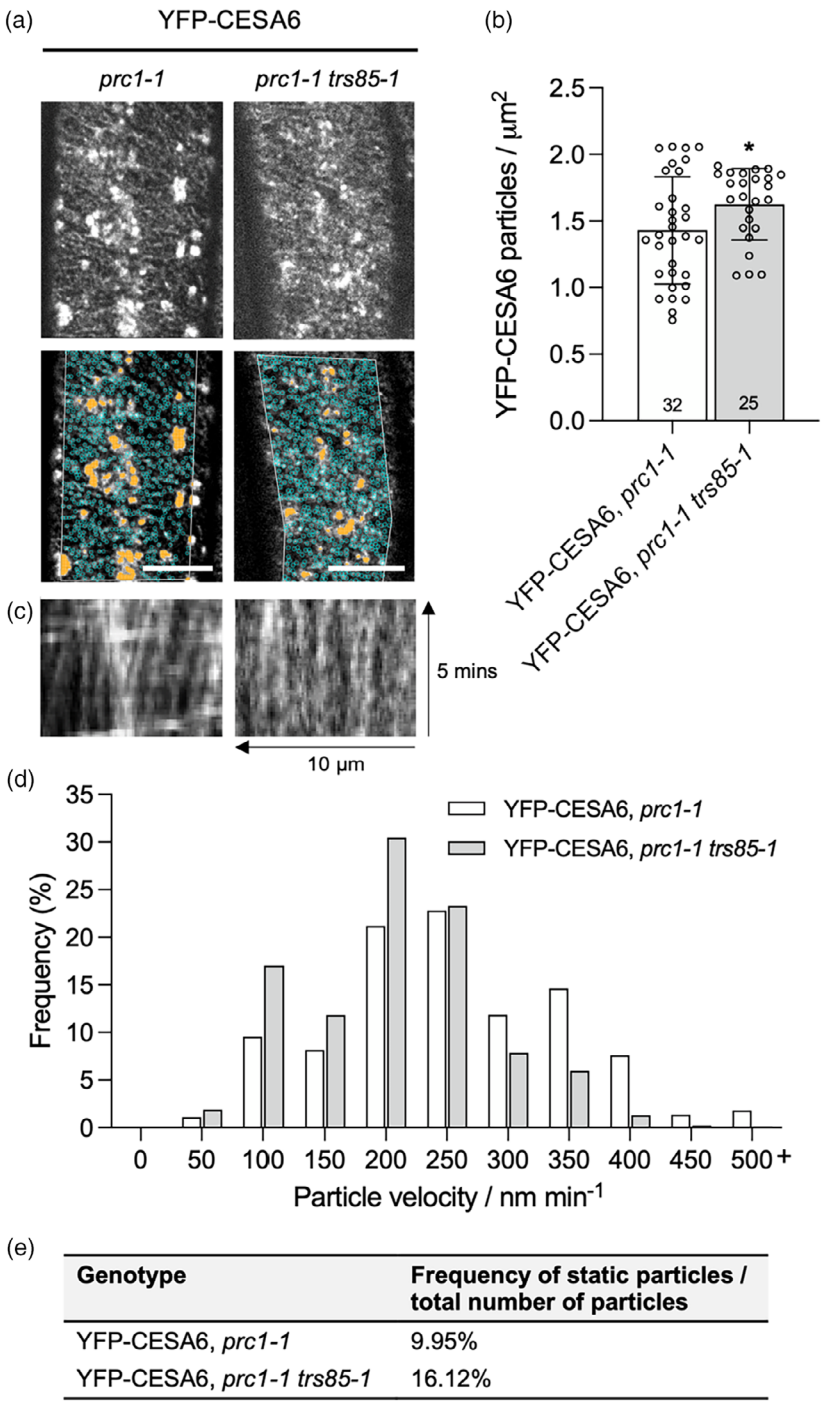

Figure 3. YFP-CESA6 dynamics are disrupted in *trs85-1*.

(a) Representative raw (top panel) and analysed (bottom panel) images of YFP-CESA6 at the plasma membrane in 2.5-day-old dark-grown hypocotyls. Plasma membrane particles are highlighted by cyan circles and cytosolic particles are shown in orange. The scale bars indicate 10 μm.

(b) YFP-CESA6 density. Asterisks indicate significance based on a t-test (*$P \leq 0.05$). Numbers on bars indicate number of images analysed. Bars show mean ± standard deviation.

(c) Representative kymographs from 5-min films taken at 5 sec intervals.

(d) Histogram of YFP-CESA6 velocity. Average velocities = YFP-CESA6, *prc1-1*: 252.2 ± 94.52 SD nm min^{-1} (n = 3268, 11 films), YFP-CESA6, *prc1-1 trs85-1*: 205.1 ± 73.68 SD nm min^{-1} (n = 3370, 10 films). The final bin represents bins 500–750 sec.

(e) Frequency of static YFP-CESA6 particles detecting during the velocity analysis. Frequency was calculated as the number of static particles divided by the total number of particles detected in the velocity analysis. Absolute frequencies = YFP-CESA6, *prc1-1*: 361 (n = 3269), YFP-CESA6, *prc1-1 trs85-1*: 648 (n = 4018).

(e)

Genotype	Frequency of static particles / total number of particles
YFP-CESA6, *prc1-1*	9.95%
YFP-CESA6, *prc1-1 trs85-1*	16.12%

Clathrin light chain dynamics are altered in *trs85-1*

We sought to investigate whether defective endocytosis may contribute to the increase in static YFP-CESA6 particles at the plasma membrane in *prc1-1 trs85-1* observed in the velocity and delivery analyses (Figures 3e and 4d), since exocytosis and endocytosis may be linked as a self-regulating feedback loop (Allen et al., 2021). Furthermore, a previous study demonstrated that Trs85 has a role in endocytosis in the *Arabidopsis* root, through reduced internalization of FM4-64 (Song et al., 2020). FM4-64 is an amphiphilic tracer that instantly stains the plasma membrane and then becomes internalized via endocytotic vesicles and, therefore, can be used to trace endocytosis from the plasma membrane (Rigal et al., 2015). After 1 h of treatment with FM4-64, no labelling of endocytotic compartments was observed in *trs85-1* (referred to as *dqc-2*) in

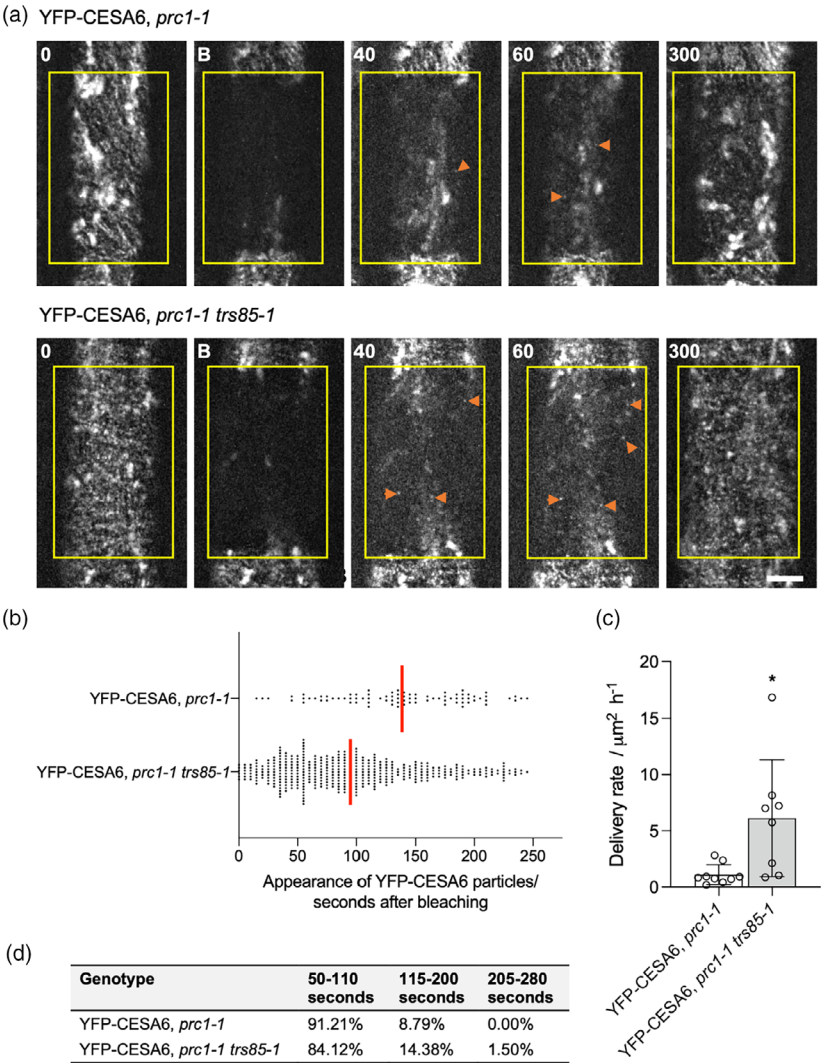

(d)

Genotype	50-110 seconds	115-200 seconds	205-280 seconds
YFP-CESA6, *prc1-1*	91.21%	8.79%	0.00%
YFP-CESA6, *prc1-1 trs85-1*	84.12%	14.38%	1.50%

Figure 4. YFP-CESA6 delivery to the plasma membrane is increased in *trs85-1*.
(a) Snapshots of cells at different time points during CSC delivery after FRAP. 0 = sec before photobleaching, B = time of photobleaching, and 40, 60, 300 = sec after bleaching. Yellow boxes indicate photobleached area and orange arrowheads represent the appearance of new YFP-CESA6 particles. The scale bar indicates 10 µm.
(b) Time needed for YFP-CESA6 particles to appear after photobleaching in seconds. Average is indicated by a red line = YFP-CESA6, *prc1-1*: 138 sec ± 55.79 SD (n = 83), YFP-CESA6, *prc1-1 trs85-1*: 95 sec ± 59.46 SD (n = 392).
(c) Delivery rate of CSCs to the plasma membrane. Average delivery rate = YFP-CESA6 *prc1-1*: 1.11 ± 2 (n = 9), YFP-CESA6 *prc1-1 trs85-1*: 6.12 ± 2 (n = 8). Asterisks indicate significance based on a t-test (*P = 0.014). Bars show mean ± standard deviation.
(d) Frequency of YFP-CESA6 particle pause phase lengths in seconds.

contrast to the wild-type that displayed clear punctate labelling of endocytotic vesicles (Song et al., 2020). We found that this difference in FM4-64 internalization was observable after just 5 min of FM4-64 treatment in the meristematic region of root epidermal cells (Figure S4).

While FM4-64 is a useful tool to study endocytosis in general, it is difficult to track individual CME events. Studies have revealed that the internalization of CSCs occurs via CME (Bashline et al., 2013, 2015). To study CME events in more detail, we crossed a red fluorescent tagged clathrin light chain protein (CLC-mOrange) with *trs85-1*. CLCs are required for the formation of clathrin-coated vesicles during CME (Konopka et al., 2008). Punctate CLC-mOrange particles appear at the plasma membrane and then disappear shortly afterwards. The appearance of CLC-mOrange particles is thought to represent the formation of clathrin-coated pits and the disappearance coincides with the scission of clathrin-coated vesicles (Bashline et al., 2015; Konopka et al., 2008). We found that the density of CLC-mOrange particles was 10% lower in *trs85-1* compared to the wild-type (Figure 5a,b), which is suggestive of fewer CME events. We also found that the lifetime of CLC-mOrange particles was on average 1 sec longer than in the wild-type (Figure 5c; Movie S4). A decrease in the density of CLC-mOrange particles coupled with an increase in average CLC-mOrange lifetime is suggestive of slower and less frequent endocytotic events in *trs85-1*. Furthermore, abnormally long CLC lifetimes over 30 sec are more common in *trs85-1*, consistent with CME deficiencies (Table S2). Therefore, we hypothesize that defective endocytosis may be partially responsible for the large increase in static YFP-CESA6 particles at the plasma membrane in *trs85-1*.

DISCUSSION

TRAPP complexes are known to be highly important for mediating protein transport between major organelles in yeast, metazoans (Barrowman et al., 2010; Kim et al., 2016) and more recently, plants (Ravikumar et al., 2018; Rosquete

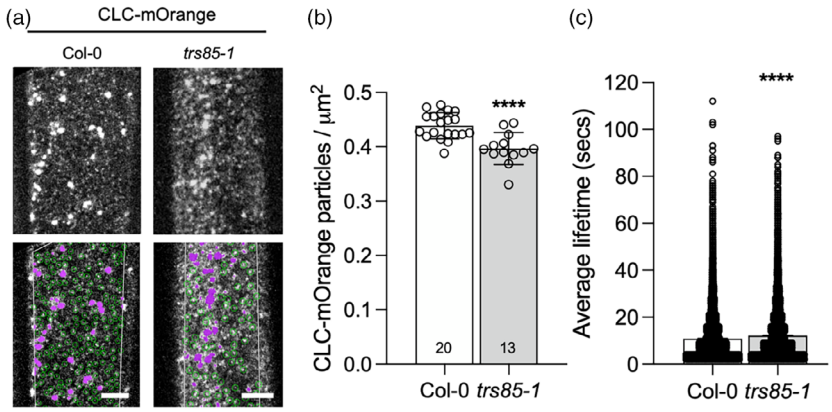

Figure 5. Clathrin-mediated endocytosis is reduced in *trs85-1*.
(a) Representative images of CLC-mOrange at the plasma membrane in 2.5-day-old dark-grown hypocotyls. Punctate CLC-mOrange labeled dots at the plasma membrane are circled in green and cytosolic particles are shaded in purple. The scale bars indicate 5 μm.
(b) CLC-mOrange density. Average density: CLC-mOrange, Col-0 = 0.44 and, CLC-mOrange, *trs85-1* = 0.40. Asterisks indicate significance based on a *t*-test (****$P \leq 0.0001$). Numbers on bars indicate number of images analysed. Bars show mean ± standard deviation.
(c) Average CLC-mOrange particle lifetimes: CLC-mOrange, Col-0 = 11 ± 3 sec (n = 11 695, eight films) and CLC-mOrange, *trs85-1* = 12 ± 3 sec (n = 10 130, five films). Each circle represents an individual data point. Asterisks indicate significance based on a *t*-test (****$P \leq 0.0001$).

et al., 2019; Rybak et al., 2014). The trafficking of CSCs has often been found to rely on proteins involved in major trafficking pathways described in eukaryotes, such as components of CME (Bashline et al., 2013, 2015), the exocyst complex (Zhu et al., 2018), Rab GTPases (He et al., 2018) and syntaxins (Drakakaki et al., 2012). Since the formation of the cell wall is an integral part of plant development, it is perhaps unsurprising that CSC regulation is dependent on these major trafficking pathways. In this study, we have found that Trs85, a subunit of the TRAPPIII complex in plants also plays a role in both the delivery and endocytosis of CSCs from the plasma membrane.

CSC delivery is enhanced in *trs85-1*

Populations of CSCs at the plasma membrane are regulated by a balance between endocytosis and exocytosis, so deviances from the expected density of CESA proteins imply that one, or both, of these pathways could be compromised. In *prc1-1 trs85-1*, we found that a higher density of YFP-CESA6 is caused by defects in both exocytosis and endocytosis. The delivery rate of YFP-CESA6 particles to the plasma membrane was almost five-fold higher in *prc1-1 trs85-1* than in *prc1-1* (Figure 4). Furthermore, YFP-CESA6 tended to be delivered 50 sec earlier in *prc1-1 trs85-1* suggesting an enhanced rate of delivery. Although we removed YFP-CESA6 particles that had an abnormal pause phase, it is likely that some atypical CSC insertion events remained in our analysis and contributed to the increased delivery rate in *prc1-1 trs85-1*. Many proteins have been reported to positively regulate CSC exocytosis, including STELLO, SEC5, PATROL1 and TRANVIA (Vellosillo et al., 2021; Zhang et al., 2016; Zhu et al., 2018). So far, only SHOU4 has been shown to negatively regulate CSC delivery (Polko et al., 2018), potentially through direct binding with CESA proteins. Whilst *shou4* and *shou4-l* mutants exhibited an increased density of CESA proteins at the plasma membrane, they did not exhibit a simultaneous increase in crystalline cellulose content, similar to *trs85-1* (Figures 2b and 3b). Increased density of CSCs is not always indicative of increased cellulose content, possibly because the density of CSCs is not a limiting factor for cellulose synthesis and increased density may even cause reduced synthesis. For instance, crowded CSCs may not be able to form cellulose microfibrils as efficiently in primary cell walls. In secondary cell walls, cellulose microfibrils tend to be highly bundled and this aggregation is directly related to the density of CSCs (Li et al., 2016). However, in primary cell walls, microfibrils tend to be less aggregated and CSCs are more sparsely distributed. This is likely to facilitate the sliding of microfibrils during growth (Cosgrove, 2022). Therefore, in primary cell walls, increased CSCs density may disrupt sparse cellulose microfibril deposition and hinder growth. Furthermore, there may be a higher density of defective CSCs at the membrane in *trs85-1* mutants that have not been sent for degradation. Trs85 is known to be important during autophagy in yeast (Lynch-Day et al., 2010) and rice (Wu et al., 2023) and so may also be involved in CSC degradation in *Arabidopsis*.

CME is reduced in *trs85-1*

Additionally, increased CSC density could represent a larger population of non-functioning CSCs that are undergoing slower endocytosis. Low crystalline cellulose content coupled with a dense population of CSCs at the plasma membrane is typically a strong indicator of defective CSC

endocytosis (Bashline et al., 2015). Mutations in Trs85 are known to cause defects in general endocytosis (Song et al., 2020), but it was not clear whether Trs85 impacts CME events. We observed both a decrease in CLC density and an increase in CLC lifetime at the plasma membrane in *trs85-1*, indicative of reduced and slower CME events (Figure 5). Although, CLC lifetimes are only 1 sec longer on average in *trs85-1*, abnormally long CLC lifetimes over 30 sec are more common in *trs85-1*, suggesting a tendency towards longer, potentially abortive endocytotic events (Table S2). Lesions in CME components such as AP2M and TWD40-2 led to the overaccumulation of CESA at the plasma membrane (Bashline et al., 2015), and this is consistent with the higher density of CSC in *trs85-1*. Although Trs85 does not co-precipitate with CLC proteins (Heard et al., 2015), it remains to be tested whether Trs85 impacts CME via other CME components.

Increase in static population of YFP-CESA6 particles in *trs85-1*

In our velocity analysis, we detected more static YFP-CESA6 particles in *prc1-1 trs85-1* than *prc1-1* (Figure 3e). We also found that after photobleaching, YFP-CESA6 particles with an atypical pause phase of over 110 sec were almost 50% more abundant in *prc1-1 trs85-1* than *prc1-1* (Figure 4d). CESA6 particles that remain static at the plasma membrane have also been reported in exocytosis mutants (Zhu et al., 2018), endocytotic mutants (Bashline et al., 2015) and transgenic lines that have point mutations in the catalytic domain of YFP-CESA6 (Huang, 2022). These static particles likely represent unsuccessful insertion events, delayed endocytotic events, or the insertion of functionally inactive CSCs. Reductions in CME coupled with unsuccessful insertions during enhanced YFP-CESA6 delivery are likely responsible for the abundance of static particles in *trs85-1*.

It is likely that a combination of endocytosis and exocytosis defects is responsible for the increased YFP-CESA6 density at the plasma membrane and the appearance of atypical, static YFP-CESA6 particles. Since endocytosis and exocytosis are interdependent processes that feedback on each other, it is hardly surprising that there are genes contributing to both trafficking pathways. For instance, CSI1 is known to have roles in both the successful delivery and removal of CSCs from the plasma membrane (Lei et al., 2015; Zhu et al., 2018). In yeast, Trs85 has been implicated in both pathways, in addition to its role in autophagy. Knock-out *trs85*Δ yeast mutants exhibit increased secretion of an ER resident protein, Kar2, outside of the cell compared to the wild-type (Thomas et al., 2018) and, Snc1, a reporter that recycles between the EEs and plasma membrane via the Golgi, accumulates in the cytosol in *trs85*Δ (Montpetit & Conibear, 2009).

What is the role of Trs85 in trafficking in *Arabidopsis*?

Previous studies in plants have shown that TRAPPIII complexes associate with the TGN/EE. Trs85 and TRAPPC11, another large TRAPPIII-specific component, co-purify with SYP61, a key marker of the TGN/EE (Drakakaki et al., 2012). Mutations in these genes' compromises TGN/EE integrity and the localization of TGN/EE markers: SYP61, SYP41, RABD2a (Rosquete et al., 2018; Song et al., 2020). Trs85 has also been identified in the membrane fraction of affinity purified RAB-D2a/ARA5 fraction representing the Golgi, TGN/EE and post-Golgi secretory vesicles, and RABG3f that represents the multi-secretory body and tonoplast secretory vesicles (Heard et al., 2015). The appearance of Trs85 in many different organelles reinforces the idea that Trs85 is important in multiple stages of the CSC trafficking pathway.

The function of Trs85 during trafficking is likely mediated through its activation of Rab1 GTPases. In yeast, Trs85 is required for binding Ypt1 both *in vivo* and *in vitro* and Ypt1 exhibits mis-localization to the Golgi in *trs85*Δ mutants (Thomas et al., 2018). Trs85 has a conserved amphiphatic helix in its C-terminal that is essential for both securing TRAPPIII complexes to the membrane and activating Ypt1 (Joiner et al., 2021). In multicellular organisms, Trs85 contains an additional 600 residues at the C-terminal that are not present in yeast (Galindo et al., 2021), suggesting that perhaps it has a unique function. A cryo-EM reconstruction of the TRAPPIII complex in *Drosophilia* predicted that this C-terminal 'arm' of Trs85 operates as a part of flexible gating system to regulate access of Rab1 to the active site because the C-terminal arm of Trs85 contacts Rab1 molecules *in vitro* (Galindo et al., 2021). Since Ypt1/Rab1 recruits vesicle tethering factors to initiate membrane fusion (Lipatova et al., 2012; Suvorova et al., 2002), insufficient activation of Rab1 homologs in *trs85-1* mutants may prevent the fusion of CSCs with the plasma membrane, producing a population of static, uninserted CSCs. Likewise, reduced Rab GTPase activation in the tonoplast and TGN/EE, where Trs85 has been identified (Drakakaki et al., 2012; Heard et al., 2015), may disrupt the trafficking of endocytosed CSCs for degradation or recycling. Inevitably this would need to be studied in further detail as the RabD family in *Arabidopsis*, which is homologous to Ypt1/Rab1, has not yet been associated with CSC trafficking. So far only RabH1b has been described in CSC trafficking, though *rabh1b* mutants exhibit similar defects to *trs85-1* including reduced CESA6 motility, reduced cellulose content and reduced endocytosis (He et al., 2018).

TRAPPII complexes in *Arabidopsis* differ from mammals as they require an additional subunit, TRIPP, to function (Garcia et al., 2020) and the same may be true for TRAPPIII complexes. It could also be possible that Trs85 works in isolation in *Arabidopsis* or part of a subcomplex.

Regardless of its role as part of a TRAPP complex, Trs85 is clearly important in mediating the endocytosis and exocytosis of CSCs in *Arabidopsis*.

EXPERIMENTAL PROCEDURES

Growth conditions

Arabidopsis thaliana seeds were sterilized with 30% bleach (v/v), rinsed thoroughly with autoclaved water and cold-stratified at 4°C in the dark for a minimum of 3 days. Stratified seeds were grown vertically on plates containing 1/2 Murashige and Skoog (MS) media, 0.05% MES and 0.8% agar (w/v) (pH 5.7). Dark-grown seedlings were grown at 22°C for 2–4 days depending on the experiment. Light-grown seedlings were grown on MS plates supplemented with 1% sucrose at 22°C under a 16-h light/8-h dark cycle for 7–10 days. For analyses on adult plants, 10-day-old seedlings were transplanted to soil and grown under the same light conditions as light-grown seedlings, for 6–8 weeks.

Plant material

The T-DNA insertion lines *trs85-1* (SALK_208572) and *trs85-2* (SALK_130580) were obtained from the Arabidopsis Biological Resource Center. YFP-CESA6 *prc1-1* (Paredez et al., 2006), CLC-mOrange (Konopka et al., 2008) and *prc1-1* (Desnos et al., 1996), were previously described. YFP-CESA6 *prc1-1*, and CLC-mOrange was crossed into the *trs85-1* background. Homozygous genotypes for *trs85-1* were confirmed by PCR, and for *prc1-1* a PCR was used followed by a restriction digestion with HpyCH4V (Table S3; Figure S3).

Live-cell imaging and analysis

For all live-cell imaging experiments, 2 to 2.5-day-old etiolated seedlings were mounted with ddH_2O and positioned between two coverslips for imaging. All images and movies were taken from the epidermal cells approximately 2 mm below the apical hook. Imaging was performed on a Yokogawa CSUX1 spinning-disk system as previously described (Li et al., 2012). A three-line laser merger with 445, 488 and 561 nm lasers was used with band-pass filters for emission filtering. Images were captured with an exposure time of 300 msec and laser intensity of 10% in the 488 nm channel or 15% in the 561 nm channel. Images were captured using Metamorph (Molecular Devices), and later analysed with either Fiji (ImageJ software, San Jose, CA, USA) (version 2.3.0/1.53q) or the Python-based program, Dot Scanner (https://github.com/bdavis222/dotscanner). All analyses were performed on raw, unmanipulated data and the contrast of the images was increased only during the production of the figures for display purposes, unless otherwise specified.

All density analyses were quantified using the Python-based program, Dot Scanner (https://github.com/bdavis222/dotscanner). In brief, fluorescent particles were detected in images if they had signal within a square area of three pixels wide and three pixels tall for YFP-CESA6 particles and a square seven pixels wide and seven pixels tall for CLC-mOrange particles which was selected to more accurately capture particles. The program also detected the area of cytosolic labelled particles. A region was selected for the analysis and all cytosolic labelled areas were subtracted from the total area of density calculated and the density was measured as the number of particles per px^2 that was then converted to μm^2 using a scale factor of 149 nm per pixel. For YFP-CESA6 density calculations, 32 images were analysed from 13 YFP-CESA6 *prc1-1* seedlings and 25 images were analysed from 13 YFP-CESA6 *trs85-1 prc1-1* seedlings. For CLC-mOrange density calculations, 20 images were analysed from nine CLC-mOrange, wild-type seedlings and 13 images were analysed from six CLC-mOrange *trs85-1* seedlings.

Velocity analyses were quantified in Fiji ImageJ using methods described previously (Zhu et al., 2018). For the velocity analyses, the contrast of all images was enhanced by 0.3% and the plugin 'WalkingAverage' (frames = 3) was used to help reduce some of the noise. All particles with a velocity of 0 nm min^{-1} were removed from the calculation of average velocity. Frequency of static particles was calculated as the number of particles with a velocity of 0 nm min^{-1} divided by the total number of particles detected in the velocity analysis. Particles were analysed from 11 YFP-CESA6 *prc1-1* films and 10 YFP-CESA6 *prc1-1 trs85-1* films. For CLC-mOrange lifetimes, 2-min movies were taken at 1 sec intervals. All particle lifetime analyses were quantified using the Python-based program, Dot Scanner (https://github.com/bdavis222/dotscanner). In brief, lifetimes were calculated as the number of consecutive frames a single CLC-mOrange particle remained in a square area of seven pixels wide and seven pixels tall. We also allowed for particles to be 'missing' from up to three frames between detected particles in the same square region since confocal imaging is prone to shifts that cause particles to come in and out of focus. We removed all particles with a lifetime of 1 sec from our analysis as we felt these were unlikely to represent true endocytotic events (Col-0 = 4910/16605 and *trs85-1* = 3533/13663).

For FRAP experiments, a region of 200 × 80 px^2 was preselected for photobleaching using the $iLAS^2$ system (Roper Scientific). After filming for 10 sec at 2 sec intervals, the defined region was photobleached, and subsequent images were taken at 5 sec intervals for a total of 5 min. The time of particle appearance following photobleaching and the length of the pause phase of newly delivered particles were calculated using the Python-based program, Dot Scanner (https://github.com/bdavis222/dotscanner). A single CSC insertion event was defined as a YFP-CESA6 particle that paused within a square area of five pixels tall and five pixels wide region for 80 ± 30 sec, before moving along a straight trajectory, in accordance with previous studies (Gutierrez et al., 2009; Zhu et al., 2018). All YFP-CESA6 particles with a pause phase outside of this range were removed from the analysis. Particles with a pause phase of 80 ± 30 sec were manually screened to see if they showed a straight trajectory. We also allowed for particles to be 'missing' from up to two frames between detected particles in the same square region, to account for shifts in the focal plane. For the delivery rate, the number of single CSC insertion events in a user-specified region was calculated over 5 min. The delivery rate was analysed in nine films from eight YFP-CESA6 *prc1-1* seedlings and eight films from seven YFP-CESA6 *prc1-1 trs85-1* seedlings..

Drug treatments

For FM4-64 labelling, 5-day-old light-grown seedlings were incubated with 1 μM FM4-64 dissolved in ½ MS liquid media with 1% sucrose for 5 min on a rocker. Stained seedlings were then mounted with ½ MS liquid media between two coverslips and then the epidermal cells of the meristematic zone of the roots were immediately imaged with a Yokogawa CSUX1 spinning-disk system as described above.

In vitro pull-downs

Full-length coding sequences of every TRAPP gene were amplified using gene-specific primers (Table S3) and cloned into the pGEX-

KG vector backbone by In-Fusion Cloning (Takara Bio). An empty pGEX-KG vector was used for the GST control. Correct plasmids were transformed into BL21-DE3 *Escherichia coli* cells. Fifty milliliters of cultures were incubated at 37°C until the OD_{600} was between 0.6 and 0.8 and then were induced at 18°C for 4 h following 1 mM isopropyl β-D-1-thiogalactopyranosid application. His-CSI1 was cloned and induced at 15°C as described previously (Zhu et al., 2018). The empty His-tag vector is pCold-TF (TaKaRa, Kusatsu, Shiga, Japan). Induced proteins were purified using glutathione beads for GST-tagged proteins and Ni-charged beads for His-tagged proteins. Soluble His-tagged proteins were subsequently eluted with 50 mM NaH_2PO_4, 300 mM NaCl and 250 mM imidazole (pH 8.0). Pull-downs were performed as described previously (Zhu et al., 2018), except that each interaction consisted of 2 μg eluted His-tagged proteins incubated with 2 μg of GST-tagged proteins conjugated to glutathione beads. Protein was extracted from the glutathione beads and subsequently analysed using SDS-PAGE gels and Western blotting. Coomassie-stained SDS-page gels were also performed side by side as a loading control. His-tagged protein signal was determined on film by chemiluminescence with a horseradish peroxidase-conjugated His antibody (1:10 000 dilution in TBST) and SuperSignal West Femto substrate (ThermoFisher Scientific).

Crystalline cellulose content

For assessing cellulose content in the primary cell wall, cell walls were extracted from 4-day-old etiolated *Arabidopsis* seedlings with 70% ethanol, and ground into a fine powder with a ball mill. Cellulose content was measured by the Updegraff method in at least five technical replicates for each genotype, as described previously (Bashline et al., 2015). Secondary cell wall cellulose content was assessed from three-inch long stem material taken from the base of 6-weeks-old plants according to Kumar and Turner (2015), in five independent adult plants for each genotype.

ACKNOWLEDGEMENTS

We thank S. Bednarek for providing the CLC-mOrange line. This work was supported by the National Science Foundation (NSF, #1951007).

CONFLICT OF INTEREST

The authors declare no conflicts of interest.

DATA AVAILABILITY STATEMENT

All relevant data can be found within the manuscript and its supporting information. Genetic materials can be accessed by contacting the corresponding author.

SUPPORTING INFORMATION

Additional Supporting Information may be found in the online version of this article.

Figure S1. Loading controls for *in vitro* interactions between CSI1 and TRAPPIII complex proteins.

Figure S2. *trs85-1* T-DNA insertion lines.

Figure S3. Genotyping of homozygous T-DNA insertion lines.

Figure S4. FM4-64 labelling of light-grown seedlings.

Table S1. Co-immunoprecipitation of TRAPP complex subunits using GFP-tagged CSI1 as bait.

Table S2. Frequency of CLC-mOrange lifetimes in seconds.

Table S3. List of primer sequences used for cloning, genotyping T-DNA insertion lines and RT-PCR.

Movie S1. The movement of YFP-CESA6 particles at the plasma membrane.

Movie S2. Examples of static YFP-CESA6 particles in *trs85-1 prc1-1*, detected during the velocity analysis.

Movie S3. The delivery of YFP-CESA6 particles to the plasma membrane assessed as fluorescence recovery after photobleaching.

Movie S4. The appearance and disappearance of CLC-mOrange particles at the plasma membrane.

REFERENCES

Allen, H., Wei, D., Gu, Y. & Li, S. (2021) A historical perspective on the regulation of cellulose biosynthesis. *Carbohydrate Polymers*, **252**, 117022.

Barrowman, J., Bhandari, D., Reinisch, K. & Ferro-Novick, S. (2010) TRAPP complexes in membrane traffic: convergence through a common Rab. *Nature Reviews Molecular Cell Biology*, **11**, 759–763.

Bashline, L., Li, S., Anderson, C.T., Lei, L. & Gu, Y. (2013) The endocytosis of cellulose synthase in Arabidopsis is dependent on μ2, a clathrin-mediated endocytosis adaptin. *Plant Physiology*, **163**, 150–160.

Bashline, L., Li, S., Zhu, X. & Gu, Y. (2015) The TWD40-2 protein and the AP2 complex cooperate in the clathrin-mediated endocytosis of cellulose synthase to regulate cellulose biosynthesis. *Proceedings of the National Academy of Sciences of the United States of America*, **112**, 12870–12875.

Cosgrove, D.J. (2022) Building an extensible cell wall. *Plant Physiology*, **189**, 1246–1277.

Desnos, T., Orbovic, V., Bellini, C., Kronenberger, J., Caboche, M., Traas, J. *et al.* (1996) Procuste1 mutants identify two distinct genetic pathways controlling hypocotyl cell elongation, respectively in dark- and light-grown Arabidopsis seedlings. *Development*, **122**, 683–693.

Diotallevi, F. & Mulder, B. (2007) The cellulose synthase complex: a polymerization driven supramolecular motor. *Biophysical Journal*, **92**, 2666–2673.

Drakakaki, G., Van De Ven, W., Pan, S., Miao, Y., Wang, J., Keinath, N.F. *et al.* (2012) Isolation and proteomic analysis of the SYP61 compartment reveal its role in exocytic trafficking in Arabidopsis. *Cell Research*, **22**, 413–424.

Galindo, A., Planelles-Herrero, V.J., Degliesposti, G. & Munro, S. (2021) Cryo-EM structure of metazoan TRAPPIII, the multi-subunit complex that activates the GTPase Rab1. *The EMBO Journal*, **40**, e107608.

Garcia, V.J., Xu, S.-L., Ravikumar, R., Wang, W., Elliott, L., Gonzalez, E. *et al.* (2020) TRIPP is a plant-specific component of the Arabidopsis TRAPPII membrane trafficking complex with important roles in plant development. *The Plant Cell*, **32**, 2424–2443.

Gu, Y., Kaplinsky, N., Bringmann, M., Cobb, A., Carroll, A., Sampathkumar, A. *et al.* (2010) Identification of a cellulose synthase-associated protein required for cellulose biosynthesis. *Proceedings of the National Academy of Sciences of the United States of America*, **107**, 12866–12871.

Gutierrez, R., Lindeboom, J.J., Paredez, A.R., Emons, A.M.C. & Ehrhardt, D.W. (2009) Arabidopsis cortical microtubules position cellulose synthase delivery to the plasma membrane and interact with cellulose synthase trafficking compartments. *Nature Cell Biology*, **11**, 797–806.

Hála, M., Cole, R., Synek, L., Drdová, E., Pečenková, T., Nordheim, A. *et al.* (2008) An exocyst complex functions in plant cell growth in *Arabidopsis* and tobacco. *The Plant Cell*, **20**, 1330–1345.

He, M., Lan, M., Zhang, B., Zhou, Y., Wang, Y., Zhu, L. *et al.* (2018) Rab-H1b is essential for trafficking of cellulose synthase and for hypocotyl growth in *Arabidopsis thaliana*. *Journal of Integrative Plant Biology*, **60**, 1051–1069.

Heard, W., Sklenář, J., Tomé, D.F.A., Robatzek, S. & Jones, A.M.E. (2015) Identification of regulatory and cargo proteins of endosomal and secretory pathways in *Arabidopsis thaliana* by proteomic dissection. *Molecular & Cellular Proteomics*, **14**, 1796–1813.

Huang, L. (2022) The catalytic domain of cellulose synthase (CESA) is involved in vesicle trafficking and protein dynamics. *bioRxiv*. Available from: https://doi.org/10.1101/2022.04.04.487015

Joiner, A.M.N., Phillips, B.P., Yugandhar, K., Sanford, E.J., Smolka, M.B., Yu, H. *et al.* (2021) Structural basis of TRAPPIII-mediated Rab1 activation. *The EMBO Journal*, **40**, e107607.

Kalde, M., **Elliott, L.**, **Ravikumar, R.**, **Rybak, K.**, **Altmann, M.**, **Klaeger, S.** ***et al.*** (2019) Interactions between transport protein particle (TRAPP) complexes and Rab GTP ases in Arabidopsis. *The Plant Journal*, **100**, 279–297.

Kim, J., **Lipatova, Z.** & **Segev, N.** (2016) TRAPP complexes in secretion and autophagy. *Frontiers in Cell and Developmental Biology*, **20**, 4.

Konopka, C.A., **Backues, S.K.** & **Bednarek, S.Y.** (2008) Dynamics of *Arabidopsis* dynamin-related protein 1C and a Clathrin light chain at the plasma membrane. *The Plant Cell*, **20**, 1363–1380.

Kumar, M. & **Turner, S.** (2015) Protocol: a medium-throughput method for determination of cellulose content from single stem pieces of *Arabidopsis thaliana*. *Plant Methods*, **11**, 46.

Lei, L., **Singh, A.**, **Bashline, L.**, **Li, S.**, **Yingling, Y.G.** & **Gua, Y.** (2015) Cellulose synthase interactive1 is required for fast recycling of cellulose synthase complexes to the plasma membrane in *Arabidopsis*. *Plant Cell*, **27**, 2926–2940.

Li, S., **Bashline, L.**, **Zheng, Y.**, **Xin, X.**, **Huang, S.**, **Kong, Z.** ***et al.*** (2016) Cellulose synthase complexes act in a concerted fashion to synthesize highly aggregated cellulose in secondary cell walls of plants. *Proceedings of the National Academy of Sciences of the United States of America*, **113**, 11348–11353.

Li, S., **Lei, L.**, **Somerville, C.R.** & **Gu, Y.** (2012) Cellulose synthase interactive protein 1 (CSI1) links microtubules and cellulose synthase complexes. *Proceedings of the National Academy of Sciences of the United States of America*, **109**, 185–190.

Lipatova, Z., **Belogortseva, N.**, **Zhang, X.Q.**, **Kim, J.**, **Taussig, D.** & **Segev, N.** (2012) Regulation of selective autophagy onset by a Ypt/Rab GTPase module. *Proceedings of the National Academy of Sciences of the United States of America*, **109**, 6981–6986.

Lynch-Day, M.A., **Bhandari, D.**, **Menon, S.**, **Huang, J.**, **Caid, H.**, **Bartholomew, C.R.** ***et al.*** (2010) Trs85 directs a Ypt1 GEF, TRAPPIII, to the phagophore to promote autophagy. *Proceedings of the National Academy of Sciences of the United States of America*, **107**, 7811–7816.

Montpetit, B. & **Conibear, E.** (2009) Identification of the novel TRAPP associated protein Tca17. *Traffic*, **10**, 713–723.

Morgan, J.L.W., **Strumillo, J.** & **Zimmer, J.** (2013) Crystallographic snapshot of cellulose synthesis and membrane translocation. *Nature*, **493**, 181–186.

Nixon, B.T., **Mansouri, K.**, **Singh, A.**, **Du, J.**, **Davis, J.K.**, **Lee, J.-G.** ***et al.*** (2016) Comparative structural and computational analysis supports eighteen cellulose synthases in the plant cellulose synthesis complex. *Scientific Reports*, **6**, 28696.

Novick, P., **Field, C.** & **Schekman, R.** (1980) Identification of 23 complementation groups required for post-translational events in the yeast secretory pathway. *Cell*, **21**, 205–215.

Paredez, A.R., **Somerville, C.R.** & **Ehrhardt, D.W.** (2006) Visualization of cellulose synthase demonstrates functional association with microtubules. *Science*, **312**, 1491–1495.

Polko, J.K., **Barnes, W.J.**, **Voiniciuc, C.**, **Doctor, S.**, **Steinwand, B.**, **Hill, J.L.** ***et al.*** (2018) SHOU4 proteins regulate trafficking of cellulose synthase complexes to the plasma membrane. *Current Biology*, **28**, 3174–3182.e6.

Purushotham, P., **Ho, R.** & **Zimmer, J.** (2020) Architecture of a catalytically active homotrimeric plant cellulose synthase complex. *Science*, **369**, 1089–1094.

Ravikumar, R., **Kalbfuß, N.**, **Gendre, D.**, **Steiner, A.**, **Altmann, M.**, **Altmann, S.** ***et al.*** (2018) Independent yet overlapping pathways ensure the robustness and responsiveness of trans-Golgi network functions in Arabidopsis. *Development (Cambridge, England)*, **145**, dev169201.

Riedel, F., **Galindo, A.**, **Muschalik, N.** & **Munro, S.** (2018) The two TRAPP complexes of metazoans have distinct roles and act on different Rab GTPases. *Journal of Cell Biology*, **217**, 601–617.

Rigal, A., **Doyle, S.M.** & **Robert, S.** (2015) Live cell imaging of FM4-64, a tool for tracing the endocytic pathways in Arabidopsis root cells. *Methods in Molecular Biology*, **1242**, 93–103.

Rosquete, M.R., **Davis, D.J.** & **Drakakaki, G.** (2018) The plant trans-Golgi network: not just a matter of distinction. *Plant Physiology*, **176**, 187–198.

Rosquete, M.R., **Worden, N.**, **Ren, G.**, **Sinclair, R.M.**, **Pfleger, S.**, **Salemi, M.** ***et al.*** (2019) AtTRAPPC11/ROG2: a role for TRAPPs in maintenance of the plant trans-Golgi network/early endosome organization and function. *The Plant Cell*, **176**, 187–198.

Rybak, K., **Steiner, A.**, **Synek, L.**, **Klaeger, S.**, **Kulich, I.**, **Facher, E.** ***et al.*** (2014) Plant cytokinesis is orchestrated by the sequential action of the TRAPPII and exocyst tethering complexes. *Developmental Cell*, **29**, 607–620.

Sacher, M., **Jiang, Y.**, **Barrowman, J.**, **Scarpa, A.**, **Burston, J.**, **Zhang, L.** ***et al.*** (1998) TRAPP, a highly conserved novel complex on the cis-Golgi that mediates vesicle docking and fusion. *The EMBO Journal*, **17**, 2494–2503.

Song, S.-K., **Kim, Y.H.**, **Song, J.** & **Lee, M.M.** (2020) Defective quiescent center/AtTRS85 encoding a TRAPPIII-specific subunit required for the trans-golgi network/early endosome integrity is essential for the proper root development in Arabidopsis. *Journal Of Plant Biology*, **63**, 23–31.

Suvorova, E.S., **Duden, R.** & **Lupashin, V.V.** (2002) The Sec34/Sec35p complex, a Ypt1p effector required for retrograde intra-Golgi trafficking, interacts with Golgi SNAREs and COPI vesicle coat proteins. *Journal of Cell Biology*, **157**, 631–643.

Thellmann, M., **Rybak, K.**, **Thiele, K.**, **Wanner, G.** & **Assaad, F.F.** (2010) Tethering factors required for cytokinesis in Arabidopsis. *Plant Physiology*, **154**, 720–732.

Thomas, L.H., **Forsyth, V.T.**, **Šturcová, A.**, **Kennedy, C.J.**, **May, R.P.**, **Altaner, C.M.** ***et al.*** (2012) Structure of cellulose microfibrils in primary cell walls from collenchyma. *Plant Physiology*, **161**, 465–476.

Thomas, L.L., **Joiner, A.M.N.** & **Fromme, J.C.** (2018) The TRAPPIII complex activates the GTPase Ypt1 (Rab1) in the secretory pathway. *The Journal of Cell Biology*, **217**, 283–298.

Thomas, L.L., **van der Vegt, S.A.** & **Fromme, J.C.** (2019) A steric gating mechanism dictates the substrate specificity of a Rab-GEF. *Developmental Cell*, **48**, 100–114.e109.

Vandavasi, V.G., **Putnam, D.K.**, **Zhang, Q.**, **Petridis, L.**, **Heller, W.T.**, **Nixon, B.T.** ***et al.*** (2016) A structural study of CESA1 catalytic domain of Arabidopsis cellulose synthesis complex: evidence for CESA trimers. *Plant Physiology*, **170**, 123–135.

Vellosillo, T., **Dinneny, J.R.**, **Somerville, C.R.** & **Ehrhardt, D.W.** (2021) TRANVIA (TVA) facilitates cellulose synthase trafficking and delivery to the plasma membrane. *Proceedings of the National Academy of Sciences of the United States of America*, **118**, e2021790118.

Wen, T.-J., **Hochholdinger, F.**, **Sauer, M.**, **Bruce, W.** & **Schnable, P.S.** (2005) The *roothairless1* gene of maize encodes a homolog of *sec3*, which is involved in polar exocytosis. *Plant Physiology*, **138**, 1637–1643.

Wu, X.Y., **Dong, B.**, **Zhu, X.M.**, **Cai, Y.Y.**, **Li, L.**, **Lu, J.P.** ***et al.*** (2023) SP-141 targets Trs85 to inhibit rice blast fungus infection and functions as a potential broad-spectrum antifungal agent. *Plant Communications*, **5**, 100724.

Zhang, J., **Chen, J.**, **Wang, L.**, **Zhao, S.**, **Li, J.**, **Liu, B.** ***et al.*** (2018) AtBET5 is essential for exine pattern formation and apical meristem organization in Arabidopsis. *Plant Science*, **274**, 231–241.

Zhang, Y., **Nikolovski, N.**, **Sorieul, M.**, **Vellosillo, T.**, **McFarlane, H.E.**, **Dupree, R.** ***et al.*** (2016) Golgi-localized STELLO proteins regulate the assembly and trafficking of cellulose synthase complexes in Arabidopsis. *Nature Communications*, **7**, 11656.

Zhu, X., **Li, S.**, **Pan, S.**, **Xin, X.** & **Gu, Y.** (2018) CSI1, PATROL1, and exocyst complex cooperate in delivery of cellulose synthase complexes to the plasma membrane. *Proceedings of the National Academy of Sciences of the United States of America*, **115**, E3578–E3587.